Predicting intraparticle diffusivity as function of stationary phase characteristics in preparative chromatography

A. Schultze-Jena [a,b], M.A. Boon [a,*], D.A.M. de Winter [c], P.J.Th. Bussmann [a], A.E.M. Janssen [b], A. van der Padt [b,d]

[a] *Food and Biobased Research, Wageningen University and Research, Wageningen, The Netherlands*
[b] *Food Process Engineering, Wageningen University and Research, Wageningen, The Netherlands*
[c] *Hydrogeology, Utrecht University, Utrecht, The Netherlands*
[d] *FrieslandCampina, Amersfoort, The Netherlands*

ARTICLE INFO

ABSTRACT

Diffusion inside pores is the rate limiting step in many preparative chromatographic separations and a key parameter for process design in weak interaction aqueous chromatographic separations employed in food and bio processing. This work aims at relating diffusion inside porous networks to properties of stationary phase and of diffusing molecules. Intraparticle diffusivities were determined for eight small molecules in nine different stationary phases made from three different backbone materials. Measured intraparticle diffusivities were compared to the predictive capability of the correlation by Mackie and Meares and the parallel pore model. All stationary phases were analyzed for their porosity, apparent pore size distribution and tortuosity, which are input parameters for the models. The parallel pore model provides understanding of the occurring phenomena, but the input parameters were difficult to determine experimentally. The model predictions of intraparticle diffusion were of limited accuracy. We show that prediction can be improved when combining the model of Mackie and Meares with the fraction of accessible pore volume. The accessible pore volume fraction can be determined from inverse size exclusion chromatographic measurements. Future work should further challenge the improved model, specifically widening the applicability to greater accessible pore fractions (> 0.7) with corresponding higher intraparticle diffusivities ($D_p/D_m > 0.2$). A database of intraparticle diffusion and stationary phase pore property measurements is supplied, to contribute to general understanding of the relationship between intraparticle diffusion and pore properties.

1. Introduction

Diffusion inside porous structures is of relevance in fields like genomics, biofilms, drug delivery, implantable devices, contact lenses, cell- and tissue engineering, geography, petroleum recovery, heterogeneous catalysis, membrane filtration and chromatography [1-13]. Well over a hundred years of research has resulted in a wide range of definitions and quantifications of pore characteristics and diffusivity correlations, even within single scientific disciplines [14, 15]. Mass transfer, from the mobile phase into the stationary phase and back is limited by the rate in which molecules enter, exit, and move through the stationary phase. The molecular movement is particularly important when relatively large distances have to be traversed by diffusive forces [16-18]. This is often the case in preparative chromatography, where large particle diameters are desired for large volumetric feed throughput while maintaining low back pressures. The limitation of mass transfer through intraparticle diffusivity becomes even more relevant with increasing mobile phase velocity [19]. Effectively, resistance to intraparticle diffusion increases separation time [17] and thus reduces productivity. However, accurately predicting intraparticle diffusion remains challenging [17, 18].

Methods to describe intraparticle diffusivity in detail are as diverse as the fields themselves, since particular challenges, scales, and technological limitations vary in each field. In membrane ultrafiltration for instance, pore geometry is often assumed to

resemble straight cylindrical tubes with the same length as the membrane thickness [20]. Such an assumption is not valid in chromatography. The only similarity of the existing theories and models is the dependence of intraparticle diffusivity on free- or self-diffusion in bulk medium, usually described in terms of Fick diffusion. Intraparticle diffusivity is thus described as bulk diffusivity, limited through one or more constraints both inherent to pore properties as well as interplay with properties of diffusing molecules.

The reduced diffusion in porous matrices and gels is described by a number of models, both empirical and analytical. A very comprehensive model is the parallel pore model, which describes the reduction of intraparticle diffusivity through particle porosity, sterical hindrance and obstruction to diffusion [21]. Within gels, diffusion is often described on the basis of gel volume fraction and the ratio of polymer strain radius to target molecule size [22]. The identification and quantification of all parameters affecting diffusivity inside stationary phases is challenging, largely due to the interplay between different parameters. Furthermore, the definitions of these parameters leave room for different interpretations and their quantification often involves indirect measurements, approximations, and/or fitting.

Our work aims at gaining further insight into individual contributions of pore characteristics and their respective relation to intraparticle diffusivity. Intraparticle diffusivity was measured in size exclusion mode via *van Deemter* curves and compared to stationary phase properties. Stationary phases were analyzed for their porosity, apparent pore size distribution, and particle tortuosity. Electron microscopy was attempted to independently confirm pore characteristics. Intraparticle diffusivities of eight different small molecules were measured in chromatographic stationary phases of three different backbone materials. For each backbone material three different stationary phases of the same series, but with a different degree of cross-linking, were analyzed. The data was used to compare the predictive capabilities of the Mackie and Meares correlation and the parallel pore model.

2. Theoretical background

2.1. Diffusion

Diffusion is the stochastic motion of molecules. Without any constraints, the diffusive motion is called free-, self- or bulk diffusion. The net ensemble movement due to a spatial difference in concentrations can be described with Maxwell-Stefan or Fick-equations. In a thermodynamically ideal system, the diffusion coefficients of Fick and Maxwell-Stefan are identical [23]. As diffusion inside chromatographic particles is often considered to happen in dilute and ideal systems, Fick diffusion coefficients are used to describe and quantify diffusive mass transfer in chromatography. In case of diffusion within a porous medium with pore dimensions in the order of magnitude of the molecular free path, diffusivity is effectively reduced. Intraparticle diffusivity can thus be described as bulk diffusivity, limited through one or more constraints inherent to pore characteristics. Hence terms such as 'apparent-' or 'effective diffusivity' are often used. Different diffusion rates for the same molecules in a different porous structures can be explained by acknowledging that different pore structures reduce bulk diffusivity differently. In addition to that, molecules adsorbed on pore surfaces may diffuse as well, which is described as 'surface diffusion' [24, 25]. In all cases discussed here, molecular transport within the porous structures is considered to be purely diffusion driven without any contribution of convection.

Overall resistance to mass transfer inside a chromatographic column is the combined result of longitudinal diffusion along the column, eddy dispersion, external film mass transfer resistance,

mass transfer resistance inside the pores of the stationary phase, rate of adsorption and desorption as well as the friction-expansion of the mobile phase [26]. As a result, a pulse injected into the column results in a broadened peak in the eluate. Measuring the eluate concentration in time allows for the construction of a so-called *van Deemter* curve by measuring mean retention time and peak variance eluted at different linear velocities. In preparative chromatography, which generally operates at high velocities using large stationary phase particles, the overall mass transfer is generally limited by resistance to diffusion inside the porous region of the stationary phase [27]. The extend of this limitation is such, that in the linear region of a *van Deemter* curve, measured under preparative conditions, the slope is almost entirely dependent on intraparticle mass transfer resistance, which in turn can be derived from the slope of the curve, while accounting for the contribution of film mass transfer resistance [27].

2.2. Predictive models

In literature a range of both empirical and theoretical models can be found describing diffusion inside porous matrices. Generally, diffusion is always described as Fickian diffusion. In the models the ratio of intraparticle diffusivity D_p over bulk diffusivity D_m is set in relation to one or more terms describing the stationary phase or an interaction between stationary phase and diffusing molecule. The majority of predictive models use the particle porosity ε_p to correlate intraparticle diffusion to a property of the stationary phase which yields the intuitive boundaries $\lim_{\varepsilon_P \to 0} Dp/Dm = 0$ and $\lim_{\varepsilon_P \to 1} Dp/Dm = 1$. Overviews of different proposed empirical, semi-empirical, and theoretical expressions relating ε_p to intraparticle diffusion are given in [14, 28].

2.2.1. Correlation by Mackie and Meares

In chromatography the correlation of Mackie and Meares (Eq. (1)), as described by Guiochon [18], is often used. While the intuitive boundary conditions of diffusion in porous space are met, the model of Mackie and Meares, developed for electrolyte diffusion in ion-exchange membranes, takes neither characteristics of diffusing molecules nor structures and dimensions of pores into account. Yet, due to its simplicity and measurability of the single parameter particle porosity ε_p, this model offers an attractive method for a first estimation of D_p/D_m.

$$D_P = \left[\frac{\varepsilon_P}{2 - \varepsilon_P} \right]^2 D_m \tag{1}$$

2.2.2. The parallel pore model

The probably most commonly used model to relate intraparticle diffusivity to pore and molecule characteristics is the parallel pore model (Eq. (2)) [29, 30]. The model is based on the assumption that diffusivity inside a porous network is comparable to diffusion inside straight parallel cylindrical tubes, where diffusion can only take place inside the pores and not through the solid phase of the pore walls [21].

For non-adsorptive processes, the parallel pore model describes an intraparticle diffusion D_p, as bulk diffusion D_m reduced by the characteristics of the solid phase: the porosity ε_p, hindrance diffusion factor $F(\lambda_m)$, and the internal obstruction factor γ_p, all three of which have values between zero and one.

$$D_p = \varepsilon_p \cdot F(\lambda_m) \cdot \gamma_p \cdot D_m \tag{2}$$

A term describing surface diffusion is added to the parallel pore model in adsorptive processes [24, 25]. In reversed phase liquid chromatography applications, surface diffusion may become the major contributor to intraparticle diffusion [31].

2.3. Particle porosity ε_p

Particle porosity ε_p refers to the pore volume accessible to the mobile phase, inside the particles. It is important to realize the influence of different measurement methods for particle porosity. Generally, particle porosity should be measured under the same conditions as chromatographic measurement, as particle porosity is not necessarily an intrinsic particle property. Particles may be subject to swelling and/or shrinking with medium composition and temperature [16]. During adsorptive processes, particle porosity may be influenced through adsorbed molecules, which block otherwise accessible pore volume [32].

Particle porosity can be measured ex- or in situ. Two methods to measure particle porosity ex situ are electron microscopy and intrusion porosimetry with nitrogen or mercury [16, 33]. Both methods require measurements in vacuum, which potentially leads to deformation of many chromatographic stationary phases. Hence caution is required when interpreting the results [13]. In situ measurement of particle porosity ε_p in chromatographic stationary phases usually encompasses elution volume measurements of two non-retained molecules of different size: one small molecule capable of accessing the entire particle pore volume and the other a large molecule incapable of entering the particle pore volume at all. The former measures the total porosity ε_t, the latter the interparticle-, bed-, or external porosity ε_e. From these two measurements, the particle porosity is calculated with Eq. (3) [18]:

$$\varepsilon_p = \frac{\varepsilon_t - \varepsilon_e}{1 - \varepsilon_e} \tag{3}$$

2.4. Hindrance diffusion factor $F(\lambda_m)$

The second term in Eq. (2), the hindrance diffusion factor $F(\lambda_m)$, describes the drag a diffusing molecule experiences due to confinement within pore walls as well as steric exclusion [34]. For molecules larger than roughly $1/10^{th}$ of pore diameter, mobility will be markedly reduced through friction with pore walls [35]. Different relationships can be found in literature to describe this phenomenon, mostly based on the ratio of molecule to pore radii λ_m and the work of Renkin [36] and Brenner and Gaydos [25]. Dechadilok and Deen [20] improved an empirical expression which had been developed through many researchers over the years and which now fits the range of $0 \le \lambda_m \le 0.95$ (Eq. (4)). Eq. (4) was developed to describe hindered diffusion of spheres in pores of membranes in absence of convection, assuming pores to be straight and cylindrical. The width of pore size distribution is not taken into account as λ_m is calculated from the mean pore radius.

$$\begin{aligned} F(\lambda_m) = 1 &+ \frac{9}{8}\lambda_m \ln\lambda_m - 1.56034\lambda_m + 0.528155{\lambda_m}^2 \\ &+ 1.91521{\lambda_m}^3 - 2.81903{\lambda_m}^4 + 0.270788{\lambda_m}^5 \\ &+ 1.10115{\lambda_m}^6 - 0.435933{\lambda_m}^7 \end{aligned} \tag{4}$$

2.5. Internal obstruction factor γ_p

The internal obstruction factor γ_p is arguably the most ambiguous contribution to the parallel pore model. The ambiguity in literature originates from different concepts for contributing mechanisms to γ_p, which are often difficult to validate experimentally [28, 37–39]. Giddings suggested that the internal obstruction factor γ_p is the product of obstruction due to constriction $\gamma_{p,cons}$ and obstruction due to tortuosity $\gamma_{p,\tau}$ [40]. In more recent definitions the obstruction due to mesopore (2–50 nm [41]) connectivity $\gamma_{p,conn}$ is attributed to γ_p as well [6], leading to Eq. (5):

$$\gamma_p = \gamma_{p,cons} \cdot \gamma_{p,\tau} \cdot \gamma_{p,conn} \tag{5}$$

In practice γ_p may be difficult to distinguish from $F(\lambda_m)$ [42, 43]. For this reason γ_p is often used as a fitting parameter which then sums up all contributions that obstruct diffusion within the pore volume, as well as any experimental errors. While this works for retrofitting a model to a particular system, little contribution is made to fundamental understanding of the relationship of intraparticle diffusion and pore structures. Nevertheless, it is useful to discuss the three different internal obstruction factors, as it exemplifies the complexity of diffusive molecular transport through a porous material.

2.5.1. Obstruction due to constriction

Constriction describes randomly located bottlenecks in diffusion paths inside the porous matrix, which slow down molecules [37, 44]. Wiedenmann et al. [45] calculate the constriction factor $\gamma_{p,cons}$ with Eq. (6) from data obtained from three dimensional images of pore structures via x-ray tomography.

$$\gamma_{p,cons} = \frac{A_{\min}}{A_{\max}} = \frac{\pi r_{\min}^2}{\pi r_{\max}^2} \tag{6}$$

In order for Eq (6) to be of any practical use, the transport relevant radii, r_{min} the smallest and r_{max} the largest pore radius a diffusing molecule encounters in a porous matrix, must be determined. This however, is not possible without detailed information on three dimensional pore structure, which presents a technical challenge for microscopy techniques beyond the scope of this paper. Due to the complexity and interdependence of all factors contributing to γ_p, the actual value of $\gamma_{p,cons}$ cannot be validated in practice [45].

2.5.2. Obstruction due to tortuosity

Obstruction to diffusion due to tortuosity $\gamma_{p,\tau}$ of porous particles is assumed to be a constant of the porous network and independent of molecular species, according to theories proposed by Giddings [40]. The obstruction to diffusion due to tortuosity $\gamma_{p,\tau}$ was calculated from measured tortuosity τ_p via Eq. (7):

$$\gamma_{p,\tau} = \frac{1}{\tau_p^2} \tag{7}$$

Tortuosity τ_p is defined as ratio of average pore length L_p to length of the porous medium or particle diameter d_p and since $L_p > d_p$, it follows that $\tau_p > 1$ [39]. This definition makes tortuosity difficult to determine, as it is not reducible to classic measurable microscopic parameters [46]. Tortuosity can be measured via electric impedance, either inside the column [47] or from column packing material in suspension [46] and generally increases with decreasing porosity [21]. Extensive discussions on tortuosity can be found in literature, e.g. [15, 38, 39, 46, 48–56]. Tortuosities between 1 and 5 [21, 37] are found.

2.5.3. Obstruction due to connectivity

Pore interconnectivity describes the extent of communication between pores in the 3D space [57]. It is well defined in pore network models, where a number of connections is attributed to each node [58]. A definition for connectivity in situ yields a term, which is hard to quantify: "connectivity describes the average number of possible distinct paths for the molecules of a fluid impregnating the porous material to move from one site of this material to another one" [37]. The contribution of connectivity to γ_p is dependent on the size of the diffusing molecule [59]. Obstruction due to connectivity $\gamma_{p,conn}$ is primarily important to small molecules. Larger molecules get increasingly hindered through proximity to pore walls and $F(\lambda_m)$ dominates. Pore network modelling has shown that connectivity can have a large effect on γ_p [43]. It is unclear however, how connectivity can be measured in situ and how its effect can be isolated from other contributions to γ_p.

Table 1
Stationary phase series and backbone material of all stationary phases.

Stationary phase	Material	Manufacturer
Sephadex G-10	Cross-linked dextran	GE Healthcare
Sephadex G-15		
Sephadex G-25		
Dowex 50WX8	Styrene-divinylbenzene	Dow Chemical
Dowex 50WX4		
Dowex 50WX2		
Toyopearl HW-40F	Hydroxylated methacrylic polymer	Tosoh Bioscience
Toyopearl HW-50F		
Toyopearl HW-65F		

3. Materials and methods

3.1. Materials

3.1.1. Mobile phase

All experiments were conducted with a phosphate based mobile phase (25 mM Na_2HPO_4, 25 mM NaH_2PO_4, and 50 mM NaCl; all from Merck, Germany) in Milli-Q water. Viscosity was measured with a Physica MCR 301 rheometer (Anton Paar, Austria). Before use the mobile phase was filtered through a 0.45 μm Durapore® membrane filter (Merck, Germany).

3.1.2. Stationary phases

Stationary phases of three different backbone materials (dextran, styrene-divinylbenzene, and hydroxylated methacrylic polymer) were selected. For each backbone material three stationary phases of the same series and a different degree of cross-linking were selected (Table 1).

The number in the name of each stationary phase denotes the degree of cross-linking or concentration of cross-linking agent. While the *Sephadex* and *Toyopearl* stationary phases are actual size exclusion *SEC* stationary phases, the *Dowex* stationary phases are cation exchange stationary phases, that were used in SEC mode. Before final packing, the H^+ ion of the *Dowex* stationary phases was exchanged for Na^+ with 1 M NaCl. Due to the relatively high salt concentration in the mobile phase, no ionic interaction between target molecules and *Dowex* stationary phases were observed. Particle size distributions were measured via probability density curves with a Mastersizer 2000 (Malvern, UK) in phos-

phate buffer at room temperature. The Sauter diameter, or surface weighted mean diameter $d_{3,2}$, and its standard deviation was calculated from ten consecutive particle size distribution measurements. The relative standard deviation *RSD* of the particle size distribution was calculated from the weighted mean of the probability density curves recorded with the Mastersizer.

3.1.3. Target molecules

Acetone was added per volume into mobile phase and heavy water D_2O was used undiluted. All solid target molecules were dissolved in the mobile phase. Their respective concentrations, molecular weights, molecule radii and detection wavelengths (refractive index in case of dextran) are listed in Table 2. Molecular radii r_m were calculated from two equations. For small molecules, up to and including the disaccharide sucrose a spherical shape was assumed and the Stokes radius calculated from Stokes-Einstein relation. For all molecules larger than sucrose, the viscosity radius R_h was calculated from the empirical relation to molecular weight M_w given in Eq. (8) [60].

$$R_h = 0.271 M_w^{0.498} \tag{8}$$

In addition a series of analytical dextran standards *Dextran 1k* through *Dextran 400k* was used for pore size distribution measurements. NaCl was obtained from Merck, Germany, all other molecules from Sigma Aldrich, St. Louis, MO, USA.

3.1.4. Chromatographic equipment

For liquid chromatography a Wellchrom set-up with a K-1001 pump and a K-2401 RI-detector was used, all from Knauer, Germany. Further a Julabo F25 MP controlled the temperature in the column jacket and a mini Cori-Flow flowmeter (Bronkhorst, The Netherlands) measured the flow rate after the detector. Pressure drop over the column bed was measured using EZG10 pressure sensors (Knauer, Germany), injection port, valves, column, pressure sensors and detectors were connected with 0.02" PEEK tubing (Grace, Deerfield, IL, USA).

All elution peaks were measured on slurry packed *Götec* Superformance 300-10 columns (300 × 10 mm) with *tefzel* capillaries of 35 cm lengths and an inner diameter of 0.5 mm, including flow adapter with frits and filter (all Götec, Germany). Bed height varied with pressure between 29 and 21 cm, the precise bed heights of each stationary phase are listed in the supplementary material

Table 2
Target molecules, respective concentration in sample volume, molecular weight, molecular radii and detection wavelength (*RI* for refractive index).

Molecule	c (g/L)	Molecular weight (Da)	Molecule radius (nm)	Detection
D_2O	Pure	20	0.09[s]	RI
γ-aminobutyric acid	10	103	0.26[s]	210 nm
Triglycerin	5	189	0.34[s]	218 nm
Fructose	10	180	0.32[s]	RI
Sucrose	10	342	0.48[s]	RI
Maltotriose	10	504	0.60[v]	RI
Dextran 2•10^6	10	2•10^6	36.71[v]	RI
NaCl	58	58	0.13[s]	200 nm
Acetone	2% (v/v)	58	0.19[s]	260 nm
Dextran 1k	5	1,100	0.89[v]	RI
Dextran 4k	5	4,400	1.77[v]	RI
Dextran 10k	5	10,000	2.66[v]	RI
Dextran 20k	5	20,000	3.76[v]	RI
Dextran 45k	5	45,000	5.63[v]	RI
Dextran 65k	5	65,000	6.76[v]	RI
Dextran 125k	5	125,000	9.36[v]	RI
Dextran 195k	5	195,000	11.68[v]	RI
Dextran 275k	5	275,000	13.86[v]	RI
Dextran 400k	5	400,000	16.70[v]	RI

[v] viscosity radius.
[s] Stokes radius.

in Table 5. The zero length column was a *Götec* Superformance 10-10 column (10 × 10 mm) without stationary phase, top and flow adapters adjusted to create an effective bed height of 0 mm.

3.2. Methods

3.2.1. Column preparation and characterization

The column was slurry packed in two steps. The first began with phosphate buffer to settle the slurry in a ramped up profile of up to 10 mL/min for 20 minutes. In the second step the funnel for the slurry packing was removed, the flow adapter and a filter placed above the stationary phase bed and the stationary phase bed further compressed at 10 mL/min for 30 min. External porosity was measured with 10 g/L dextran with an average molecular weight of approximately 2,000,000 Da (for the purpose of clarity referred to as *dextran* $2 \cdot 10^6$), total porosity was measured with D_2O, except for the case of *Sephadex* G-10, where only acetone was available for total porosity determination. Comparison in the two other *Sephadex* stationary phases showed close similarity in retention volume for D_2O and acetone. All porosity measurements were conducted in phosphate buffered mobile phase at 25 °C. For all experiments the same mobile phase was used and no adsorption took place. Therefore, the particle porosity was assumed to remain constant for each stationary phase throughout this work. External porosity was confirmed by comparison of measured pressure drop over the column bed with the estimated pressure drop, calculated with the *Ergun* equation [61].

3.2.2. Chromatographic analysis

All chromatographic measurements were conducted as pulse injections of 80 μL. The column was kept at 25 °C through a water jacket. All peaks were analyzed with the method of moments in *Microsoft Excel* as described in [62]. Integration limits were set automatically at 1% of total peak height and baseline drift was corrected for automatically, where necessary, to mitigate common concerns of inaccuracy when using the method of moments [63-65]. *Van Deemter* curves were recorded at linear superficial velocities u_S of 0.5, 1, 2, and 3 m/h. *Sephadex* G-25 was additionally measured at $u_S = 0.2$ m/h, the *Toyopearl* stationary phases were additionally measured at $u_S = 4$ m/h. All measurements were corrected for the extra-column contribution for each mobile phase velocity and target molecule, with the zero length column as described in [62]. For comparison of data from different stationary phases and target molecules, *van Deemter* curves were normalized by dividing *HETP* by the resin particle diameter d_p, which yields the reduced HETP h and the linear interstitial velocity u_L is multiplied by d_p and divided by D_m which yields the reduced velocity ν.

3.2.3. Bulk diffusion coefficient

The bulk diffusion coefficient D_m of D_2O was taken from Eisenberg and Kauzmann [66]. Bulk diffusion coefficients of all other molecules were calculated with the correlation of Wilke and Chang, with molecular volumes calculated from the correlation of LeBas, both as described in [67]. For the estimated bulk diffusion coefficient an error of 20% was assumed.

3.2.4. Measuring intraparticle diffusivity

Intraparticle diffusivity was measured by fitting the plate height equation of the lumped kinetic model to experimental *van Deemter* curves, based on Coquebert de Neuville et al. [27], assuming a constant and homogenous distribution of ε_p. The slope was measured from the linear region of four point *van Deemter* curves (five measurement points for *Sephadex* G-25 and for the *Toyopearl* series) of *HETP* (m) over interstitial linear velocity u_L (m/s). From the slopes

of the *van Deemter* curves the lumped kinetic factor $k_{overall}$ was calculated with Eq. (9).

$$k_{overall} = \frac{\frac{2}{\frac{1-\varepsilon_b}{\varepsilon_b}} \cdot \left(\frac{k_1}{1+k_1}\right)^2}{\left(\frac{HETP}{u_L}\right)} \tag{9}$$

In size exclusion chromatography, the zone retention factor k_1 is dependent on a molecule's ability to penetrate pore volume, rather than adsorption equilibria, therefore $\varepsilon_{p.SEC}$ is used in Eq. (10), based on [42].

$$k_1 = \frac{1-\varepsilon_b}{\varepsilon_b} \cdot \varepsilon_{p.SEC} = \frac{1-\varepsilon_b}{\varepsilon_b} \cdot \frac{V_R - V_0}{V_C - V_0} \tag{10}$$

With the retention volume V_R, the void volume V_0 and the geometric column volume V_C. Intraparticle diffusivity D_p was then calculated from Eq. (11).

$$D_p = \frac{r_p^2}{15\left(\frac{1}{k_{overall}} - \frac{r_p}{3 \cdot k_{film}}\right)} \tag{11}$$

With r_p particle radius and the resistance to mass transfer through the stagnant film layer k_{film}, calculated as a function of reduced velocity $\nu = =(2 \cdot r_p \cdot u_L)/D_m$ from the correlation of Wilson and Geankoplis [68] as shown in Eq. (12).

$$k_{film} = \frac{1.09}{\varepsilon_b} \frac{D_m}{2 \cdot r_p} \nu^{1/3} \tag{12}$$

This method relies on an assumed linearity for the calculation of a constant $k_{overall}$ for the entire linear region of the *van Deemter* curve. However, since $k_{overall}$ is a function of linear velocity, as it is dependent on k_{film}, the van Deemter curve is not truly linear. We therefore calculated D_p for each measurement point of the curve and used the average of the calculated values for each *van Deemter* curve. The relative standard deviation of the D_p measurements was just below 2% for all data points.

The confidence interval of D_p was calculated from the propagated uncertainties of the slope and k_{film}. The uncertainty of the slope was calculated from the standard error of the slope with a 95% confidence interval and the uncertainty of k_{film} from an uncertainty of 20% for D_m.

3.2.5. Pore size distribution measurement

The apparent pore size distribution was measured via inverse size exclusion chromatography, based on a lognormal pore size distribution as explained in [69]. The partition coefficient K_D was calculated from the first moment of pulse injections for the target molecules listed in Table 2, using the mean retention volume V_R, the interparticle void volume V_0 and the total mobile phase volume V_T (Eq. (13)). Interparticle void volume and total mobile phase volume were measured with *dextran* $2 \cdot 10^6$ and D_2O respectively.

$$K_D = \frac{V_R - V_0}{V_T - V_0} \tag{13}$$

Eq. (14) was fitted to the plot of K_D over molecular radius r_m for each stationary phase using gProms *Modelbuilder* 4.0. Fitting parameters were r_{pore} and s_{pore} of the pore size distribution function $f(r)$ in Eq. (15). The pore shape dependent constant a was assumed to be 2 (cylindrical pores), as discussed in [70].

$$K_D = \frac{\int_{r_m}^{\infty} f(r) \left[1 - (r_m/r)\right]^a dr}{\int_0^{\infty} f(r) \, dr} \tag{14}$$

The function $f(r)$ in Eq. (15) describes the pore size distribution as a log-normal probability density function. This probability density function is completely equivalent to other, maybe more commonly used, probability density functions, with the advantage that

the fitting parameters r_{pore} and s_{pore} are the mean and standard deviation of the distribution, respectively [71].

$$f(r) = \frac{1}{r\sqrt{2\pi}} \left[\ln\left(1 + \left(\frac{s_{pore}}{r_{pore}}\right)^2\right)\right]^{-0.5} \cdot e^{\left[- \frac{\left(\ln\left(\frac{r}{r_p} \cdot \left[1 + \left(\frac{s_{pore}}{r_{pore}}\right)^2\right]^{0.5}\right)\right)^2}{2 \cdot \ln\left(1 + \left(\frac{s_{pore}}{r_{pore}}\right)^2\right)}\right]}$$

(15)

From the fitted function the K_D curve was calculated and the predicted K_D used to describe the accessible pore fraction of pore volume for each molecule based on its size.

3.2.6. Contributions to the internal obstruction factor

Tortuosity was measured via electric impedance in phosphate buffer, based on Barrande et al. [46] and Aggarwal et al. [47]. All measurements were conducted at room temperature in a conductivity cell with a *Vertex 10A* impedance analyzer and *IviumSoft* software (both by Ivium technologies, The Netherlands). Impedances were measured in phosphate buffer without stationary phase particles and in phosphate buffer with stationary phase particles sedimented into the upside-down conductivity cell. The exact value of the external porosity in the conductivity cell was not known. Bed porosity was estimated to be slightly larger than the geometric optimum of 0.34. We therefore calculated tortuosity for five different bed porosities in range of 0.36 through 0.44 and worked with the average value as well as the standard deviation. With Eq. (16) the total tortuosity τ_t was calculated from the measured impedance in sedimented stationary phase σ_t and without stationary phase σ_0.

$$\frac{\sigma_0 \cdot \varepsilon_t}{\sigma_t} = \tau_t$$

(16)

Intraparticle tortuosity was derived from particle conductivity with Eq. (17) [47].

$$\varepsilon_t \cdot \frac{2 + \frac{\sigma_p}{\sigma_0} + (1 - \varepsilon_e) \cdot \left(1 - \frac{\sigma_p}{\sigma_0}\right)}{2 + \frac{\sigma_p}{\sigma_0} - 2 \cdot (1 - \varepsilon_e) \cdot \left(1 - \frac{\sigma_p}{\sigma_0}\right)} = \tau_t$$

(17)

Using the solver add-on in *Microsoft Excel*, the intraparticle conductivity σ_p was fitted in Eq. (17), particle tortuosity τ_p was then calculated with Eq. (18).

$$\frac{\sigma_0 \cdot \varepsilon_p}{\sigma_p} = \tau_p$$

(18)

As pointed out in Section 2.5, validation of the obstruction to diffusion due to constriction $\gamma_{p,cons}$ and connectivity $\gamma_{p,conn}$ cannot be isolated and validated in practice. For the contribution of constriction and connectivity to the internal obstruction factor γ_p, the authors therefore resigned to a value of 1 in Eq. (5).

3.2.7. Visualization of stationary phases and pore structures

Two electron microscopy methods were used to visualize the presence of the pores: focused ion beam - scanning electron microscopy *FIB-SEM* and transmission electron microscopy *TEM*. Small amounts of the stationary phases were oven-dried overnight at 60 °C. The resulting powder was subsequently sprinkled onto a standard aluminum *SEM* stub with a carbon sticker on top. Following, a metallic layer *Pt* was sputter coated (Cressington, HQ280) across the stub to ensure sufficient electrical conduction.

The *FIB-SEM* (Thermo Scientific, Helios Nanolab G3-UC) combines the imaging capabilities of the *SEM* with the milling capabilities of a *FIB*. The *FIB* is a beam of gallium ions which scans the surface of a sample. The momentum transfer of the gallium ions onto a sample causes the samples atoms to disappear into the vacuum, a process called sputtering or milling. Prolonged milling results in a trench or cross section of some tens of micro meters. Subsequently, the *SEM* is employed to visualize the cross section.

Visualization is done in backscatter electron mode, which is less affected by local surface charge.

Milling and imaging was performed at customary conditions: a 30 keV ion beam, starting at 9.4 nA and gradually reducing to 40 pA for the final polishing. Prior to the milling, a small layer (1 μm) of *Pt* was deposited across the region of interest. The *Pt* deposition acts as protection against the ion beam and it smoothens the surface and therefore the finish of the cross section. Imaging polymeric samples with electron microscopy is not trivial. The low atomic weight of the polymer chains doesn't create any contrast.

The *TEM* analyzed *Dowex* 50WX2 sample was stained with 0.1 mL/g $FeSO_4$. An additional challenge is the resolving power of the *SEM*. An ideal sample can be resolved down to 0.8 nm. However, the resolving power obtained from unstained polymers is probably not better than 10 nm. Therefore, pores >10 nm can be investigated directly by *FIB-SEM*. In addition, the presence of 1-2 nm pores was therefore investigated by transmission electron microscopy *TEM*. *TEM* requires a thin sample of no more than 100 nm thick, which were made by the *FIB-SEM*. Again standard procedures were followed. The final polishing step was done at 30 kV, 40 pA. The *TEM* (Thermo Scientific, Talos F200x) in STEM mode, using the High Angular Annular Dark Field *HAADF* detector.

3.2.8. Note on availability of data

In an effort to support the understanding of intraparticle diffusivity and its relation to stationary phase characteristics, all of the measured data is made available in the supplementary material of this manuscript.

4. Results and discussion

4.1. Intraparticle diffusion

Intraparticle diffusion was measured in nine different stationary phases with eight different tracer molecules at the same conditions (Fig. 1). Data in Fig. 1 is grouped per backbone material, within each backbone material per decreasing cross-linking and increasing molecular size, both left to right. Determination via the slope of *van Deemter* curves gave accurate results, the majority of the error bar seen in Fig. 1 is due to the uncertainty of 20% allocated to the bulk diffusion coefficient D_m estimated with the Wilke-Chang equation. As expected, intraparticle diffusion, conveniently expressed as dimensionless ratio of intraparticle to bulk diffusion D_p/D_m, differs from stationary phase to phase and molecule to molecule. All experimental *van Deemter* curves can be found in the supplementary material (Fig. 8, Fig. 9, and Fig. 10). All elution data can be found in Tables 6-14 in the supplementary material.

Two trends are obvious in the *Sephadex* stationary phases: first, decreased cross-linking has a positive effect on intraparticle diffusivity and second, increasing target molecule size decreased intraparticle diffusivity. Both observations are easily explained by the mass transfer limiting mechanisms, where smaller molecules experience less resistance to diffusion than larger molecules and pore dimensions increase with decreasing cross-linking. The *Dowex* series, a cation exchange material, shows a similar trend in relation to the cross-linking. The same correlation with the target molecule size holds, with the exception of triglycine. Finally, in the *Toyopearl* series most of the correlations between intraparticle diffusivity, cross-linking and target molecule size are lost. *Toyopearl* HW-50F and HW-65F showed comparable measured intraparticle diffusivities. According to the manufacturer, the pore size of *Toyopearl* HW-65F is eight times larger than for HW-50F and 20 times larger than for HW-40F, a difference in pore size which was not apparent from the measured data.

Perhaps most remarkable is the relatively low intraparticle diffusivity of D_2O in comparison to larger molecules. In order to ex-
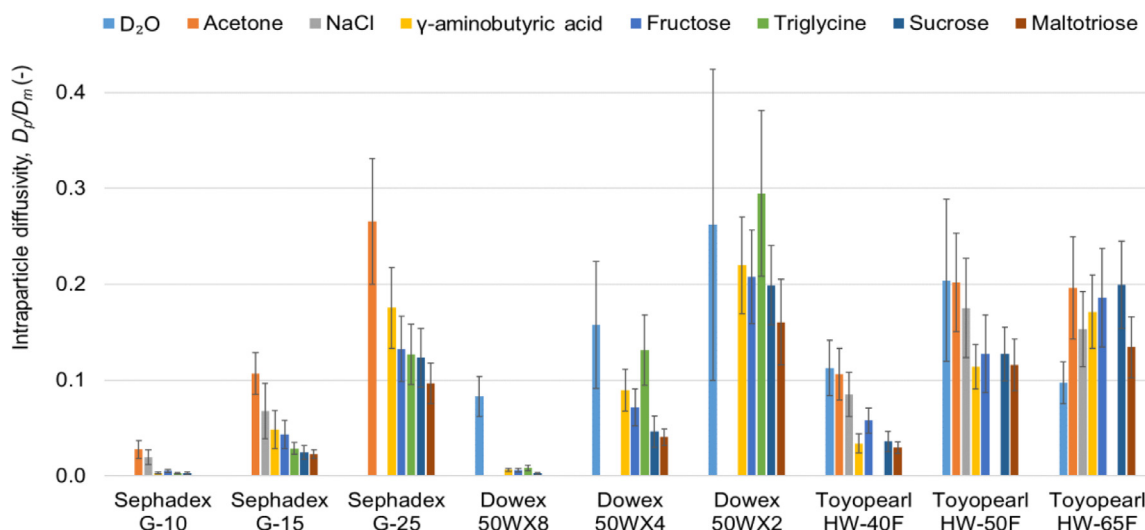
Fig. 1. Measured intraparticle diffusion ratio D_p/D_m in all nine stationary phases for all target molecules. Error bars indicate uncertainty of determination of D_p from slope of *van Deemter* curves (based on a 95% confidence interval) and 20% uncertainty of D_m estimation.

plain the observations in Fig. 1, additional information regarding the pore structure is required.

4.2. Particle size distribution and porosity

The Sauter diameter was measured in ten consecutive measurements in the Mastersizer. It was not possible to obtain all stationary phases of a series with the same particle diameter, however influence of particle size on mass transfer resistance was accounted for (an input parameter in the modelling equations, *e.g.* Eqs. (11) and (12), and by normalizing the *van Deemter* curves). The average Sauter diameters along with the measured relative standard deviations are given for each stationary phase in Table 3. Additionally, the relative standard deviation *RSD* of the particle size distribution, as measured in the Mastersizer, are given in Table 3. The measured *RSD* is between 15% and 28% for all stationary phases. Horváth et al. show that comparable *RSDs* lead to relative increases of HETP of around 5–10% for small molecules in a stationary phase with a diameter of 5 μm [72]. The effect of the particle size distribution on the slope of *van Deemter* curves and subsequent intraparticle diffusivity D_p was not included in this research. In an comparative exercise, particle diameter was additionally measured from SEM images, in the following referred to as d_{SEM}, by averaging at least 35 particles. The Sauter diameter measured with the Mastersizer and d_{SEM} differ substantially. It is likely that the particles shrank upon drying or in the vacuum chamber, as the stationary phase had not been fixated. Consequently, pore structures may have changed.

The measured particle porosities varied between 0.46 in *Sephadex* G-10 and 0.84 in *Dowex* 50WX2 and increased with decreasing cross-linking within a series, except for *Toyopearl* HW-65F, which shows a slightly smaller porosity than *Toyopearl* HW-50F (Table 3). The particle porosity for *Toyopearl* HW-65F matches data reported in literature well [69].

4.3. Visualization of pore structures

In total five of the nine stationary phases were analyzed in a FIB-SEM (*Sephadex* G-15, *Dowex* 50WX8 and 50WX2, and *Toyopearl* HW-50F and HW-65F) and one in a TEM (*Dowex* 50WX2). Examples from the outside of particles and pore structures, laid bare with a focused ion beam, can be seen in Fig. 2. Visualizing pore structures proved to be very challenging due to the very small diameters. Only the *Toyopearl* HW-65F revealed a pore structure. The absence of macro pores (pore diameters exceeding 50 nm [41]) was the only conclusion that could be drawn for the other four stationary phases analyzed in FIB-SEM. High resolution TEM imaging was only just able to reveal structures in the *Dowex* 50WX2 sample. The presented electron microscopy data is inconclusive with respect to relating intraparticle diffusivity to pore structures, given the shrinkage of particle size compared to particle size distribution measurements in phosphate buffer (Table 3).

4.4. The correlation of Mackie and Meares

The correlation of Mackie and Meares uses particle porosity as sole parameter to determine intraparticle diffusivity. It is important
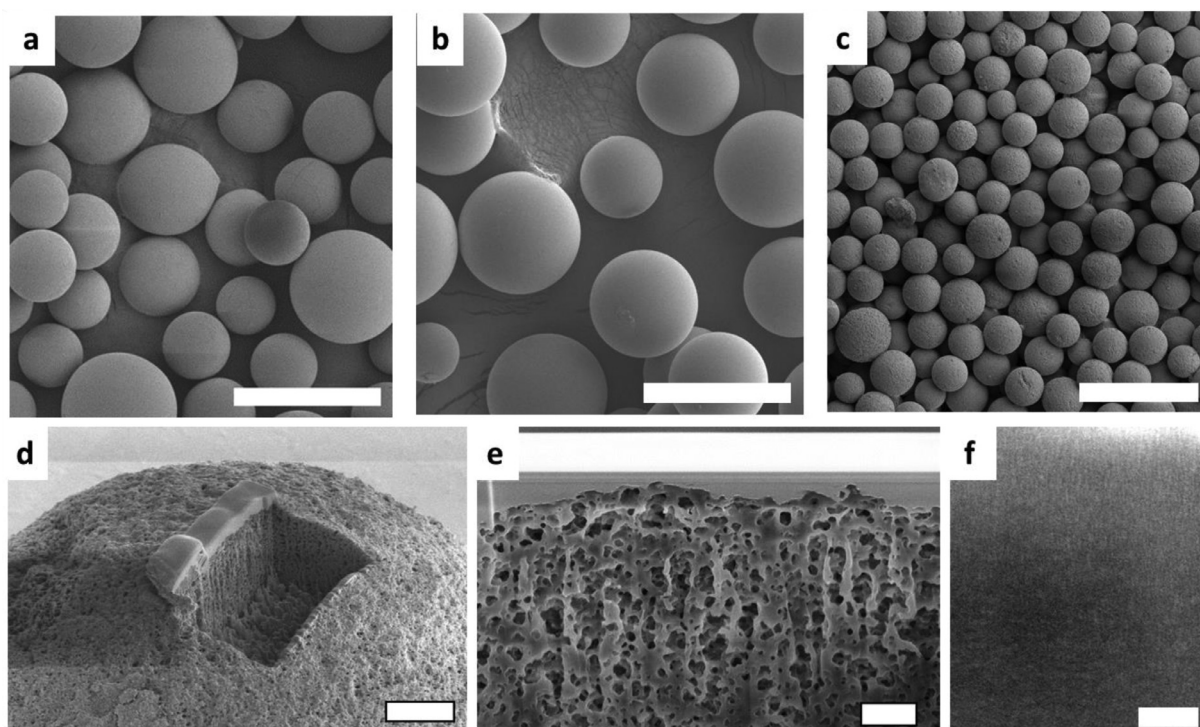
Table 3

Stationary phase series Sauter diameter and its relative standard deviation for all stationary phases. The relative standard deviation *RSD* describes the width of the particle size distribution *PSD* as measured with the Mastersizer. The particle diameter d_{SEM} was determined from electron microscopy images. Additionally measured particle porosities and apparent mean pore radii r_{pore} (from ISEC measurements as detailed in Section 4.5).

Stationary phase	Sauter diameter [μm]	RSD of PSD	d_{SEM} [μm]	Particle porosity, ε_p	r_{pore} [nm]
Sephadex G-10	88 ± 0.8%	25%	*n.d.*	0.46	1.0
Sephadex G-15	74 ± 0.2%	27%	58	0.66	1.4
Sephadex G-25	262 ± 1.1%	28%	*n.d.*	0.73	1.7
Dowex 50WX8	91 ± 0.1%	20%	71	0.52	0.7
Dowex 50WX4	106 ± 0.3%	21%	*n.d.*	0.68	1.4
Dowex 50WX2	141 ± 0.8%	19%	64	0.84	2.3
Toyopearl HW-40F	48 ± 0.4%	18%	*n.d.*	0.66	1.7
Toyopearl HW-50F	50 ± 0.1%	19%	34	0.72	5.0
Toyopearl HW-65F	52 ± 0.2%	15%	33	0.68	35.0

n.d.: not determined.

Fig. 2. Examples from the stationary phase as examined by *FIB-SEM* and *TEM*: (a) *Sephadex* G-15 (b) *Dowex* 50WX8 (c) *Toyopearl* HW-65F. (d) A *FIB* cross section was made into an individual *Toyopearl* HW-65F particle and imaged (e) by the *SEM*. The pore dimensions of the other stationary phases are of the order of 1-2 nm and can only just be made visible by *TEM* (f, *Dowex* 50WX2). Scale bars are (a-c) 100 μm, (d) 5 μm, (e) 1 μm and (f) 40 nm.

to note the role of particle porosity, as measurement with a different molecule yields very different results. A smaller molecule will have access to a different pore volume than a larger molecule [69, 73]. In this study the smallest readily available molecule, D_2O, was used for the determination of the total and particle porosity. Other studies which used same method to measure particle porosity used different molecules like a monomeric sugar, e.g. [69]. For illustration purposes, we also calculated total and particle porosity based on the retention of fructose. Fructose has roughly three times the molecular radius of heavy water. Fig. 3a and b plot the normalized intraparticle diffusivities as a function of particle porosity, based on the retention of D_2O and fructose respectively. The dashed line

indicates the Mackie and Meares correlation. The experimental results follow the expected boundaries to diffusion in porous space, as discussed in Section 2.2. However, the correlation systematically over-estimates the diffusivity values, when particle porosity is based on the retention of D_2O. Calculated particle porosities are on average 30% smaller, when particle porosity is based on the retention of fructose. In consequence measured intraparticle diffusivities match the correlation of Mackie and Meares visibly better, albeit far from perfect. This result is of little practical relevance, but it serves to emphasize the importance of ε_t and ε_p determination. We suggest the use of D_2O for particle porosity measurements, as it measures a more relevant pore spectrum for the chromato-
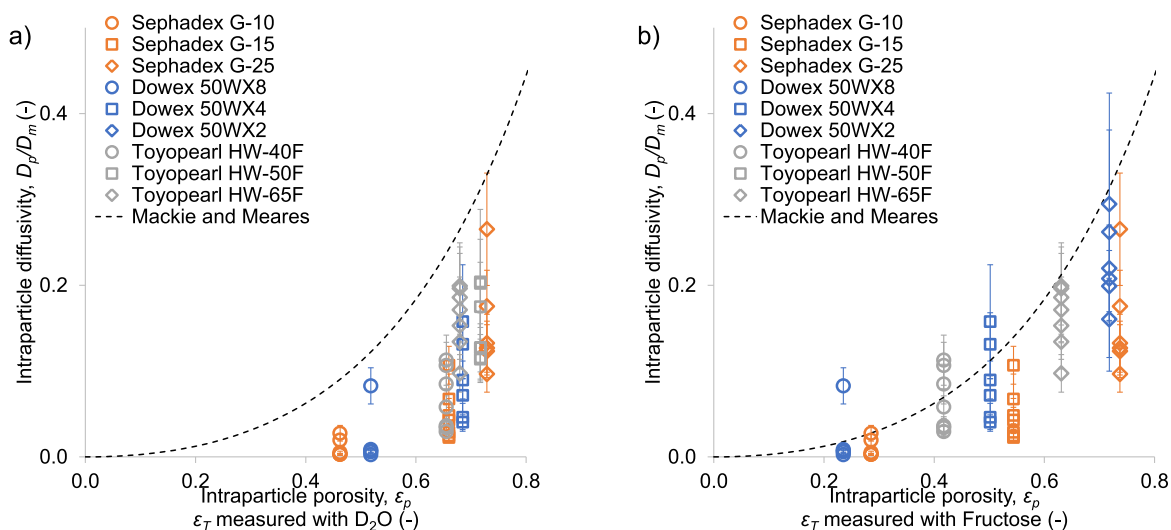

Fig. 3. Intraparticle diffusion as function of particle porosity ε_p for different molecules in nine different stationary phases and the correlation of Mackie and Meares (dotted line). (a) ε_p is based on retention of D_2O and dextran, (b) ε_p is based on retention of fructose and dextran.
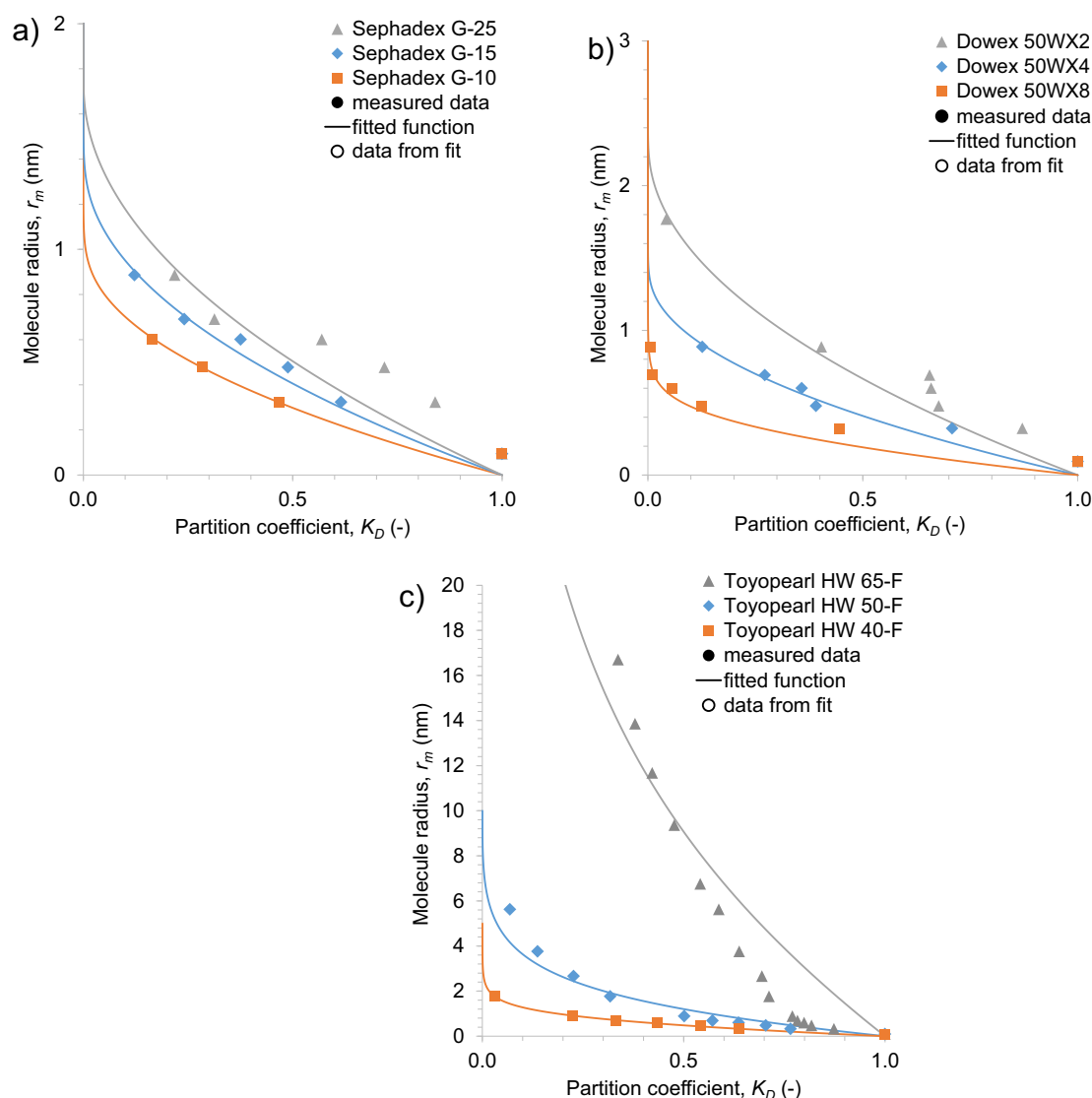
Fig. 4. K_D curves of (a) *Sephadex*, (b) *Dowex* and (c) *Toyopearl* stationary phases, relating the partition coefficient to molecular radii. Measurements (symbols) and fitted functions (solid lines). Due to the larger pores, also larger molecules were employed for the pore size measurement of the *Toyopearl* series, therefore the y-axis is scaled to a different maximum.

graphic separation of small target molecules, such as small sugars and peptides. In all following calculations ε_t and ε_p are based on the retention of D_2O.

The correlation of Mackie and Meares may serve as an early estimation of intraparticle diffusivity, but low accuracy must be assumed. From Fig. 3a can be observed that particle porosity alone is insufficient as parameter to predict intraparticle diffusivity. This is clearly reflected in the vertical distribution of intraparticle diffusivity values in Fig. 3a. A single particle porosity value can produce a range of diffusivity values, even after normalization. Additional structural properties of both the stationary phase and the target molecules are not considered.

4.5. Apparent pore size distribution

For the measurement of pore size distribution, K_D curves were recorded for each stationary phase, depicting the accessible fraction of pore volume for molecules of different sizes (closed symbols in Fig. 4a–c). Lognormal pore size distribution curves were fitted to the experimental data. Based on the underlying function (Eq. (14)) the K_D curves were calculated (lines in Fig. 4a–c).

Note, Fig. 4a–c each have a differently scaled y-axis to accommodate different pore size distributions. In general, the fitting led to a good description of the experimental data. However, for none of the resins the pore size distribution $f(r)$ of Eq. (15) could describe the D_2O data point ($K_D = 1$, $r_m = 0.09$nm). This is due to the fact that the finite size of the molecule leads to a reduction to the fraction of accessible pore volume. The small mean pore sizes fitted (Table 4) resulted even for D_2O in $K_D < 1$. It was not possible to determine the standard deviation of the pore size distribution. The fitted function is sensible to variance only in the range of very small K_D values, for $K_D \geq 0.2$ different variances are barely discernible in the function.

All data recorded during inverted size exclusion measurements can be found in Table 15, Table 16, and Table 17 in the supplementary material.

The fitted mean pore size correlate well to measured intraparticle diffusion data of Section 4.1. The *Sephadex* material shows a consistent correlation: larger pores result in higher intraparticle diffusivity. The same correlation is found for the *Dowex* series. The difference in mean pore sizes for the *Toyopearl* series is more pronounced. Both, in comparison to the other two backbone

Table 4
Fitted mean pore radii r_{pore} of pore size distribution for each stationary phase.

Stationary phase	r_{pore} (nm)
Sephadex G-10	1.0
Sephadex G-15	1.4
Sephadex G-25	1.7
Dowex 50WX8	0.7
Dowex 50WX4	1.4
Dowex 50WX2	2.3
Toyopearl HW-40F	1.7
Toyopearl HW-50F	5.0
Toyopearl HW-65F	35.0

materials, as well as the difference between *Toyopearl* HW-F40/F50 and *Toyopearl* HW-F65. Both observations are not reflected in the measured intraparticle diffusivity. For all nine stationary phases the mean of the pore size distribution increases with decreasing cross-linking.

Pore size distribution measurement via inverted size exclusion chromatography *ISEC* does not yield absolute but functional values and resulting data should be referred to as apparent pore size distribution [70]. This is partly due to a pore shape parameter within the fitting function (*a* in Eq. (14)), which requires an assumption about the pore shape [70], although it has been later shown that *ISEC* is fairly insensitive to the descriptions of pore geometry [13]. Especially in gels, where pores and pore structures are somewhat differently defined, pore size distribution measurement via *ISEC* is mainly of functional use, rather than matching the geometry of the gel [74] and can only be used to simplify description of pores in gels [75].

The *Toyopearl* stationary phase series are the only series for which pore sizes are provided by the manufacturer, however the reference does not include the measurement method for the pore radii [76]. The pore radii are 2.5, 6.3, and 50 nm for the *Toyopearl* HW40-F, HW50-F, and HW-65F respectively, the latter was also found by DePhillips and Lenhoff [69]. Mean pore radii measured in this work for the *Toyopearl* series value about 70 to 80% of the data supplied by the manufacturer, although the fitted K_D curves of *Toyopearl* HW40-F and HW50-F in Fig. 4 match measured data reasonably well. The different result highlights how much the results depend on the method used to acquire the data.

Toyopearl HW65-F is the only stationary phase analyzed in this work with observable macropores from *SEM* analysis. The viscosity radius of the largest molecule employed in this research, a dextran molecule of approximately 2,000,000 Da, is 37 nm. Thus it is likely that the dextran molecule is capable of accessing a fraction of the macro-porous pore space, which yields the measurement of external porosity inaccurate. This affects the accuracy of both of intraparticle diffusivity and measured pore size distribution as well. An even larger molecule to measure external porosity, for example large *DNA* molecules as used in [69], would certainly not be able to penetrate any pore space.

4.6. Obstruction due to tortuosity

Particle tortuosity, measured via electric impedance, shows trends within each stationary phase series, that correlate to particle porosity. With increasing particle porosity, tortuosity decreases, and the obstruction due to tortuosity $\gamma_{p,\tau}$ increases, just as predicted in literature, e.g. [21]. External porosity is unknown, but a required input factor in Eq. (17). The results in Fig. 5 show the average of the obstruction due to tortuosity $\gamma_{p,\tau}$, calculated for five assumed external porosities, as detailed in 3.2. *Contributions to the internal obstruction factor*, with the error bar as standard deviation of the five results. At similar particle porosity, the tortuosi-
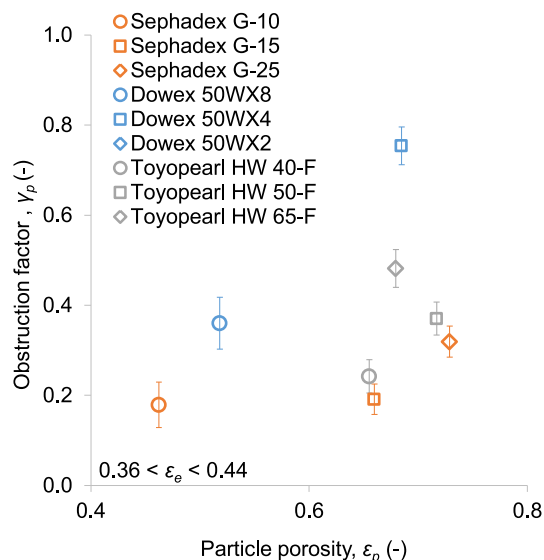

Fig. 5. Obstruction due to tortuosity calculated from particle tortuosity measured via electric impedance. Exact external porosities were unknown, therefore tortuosity was calculated for five estimated external porosities between 0.36 and 0.44. Displayed value is the average of five calculations with the standard deviation as the error bar.
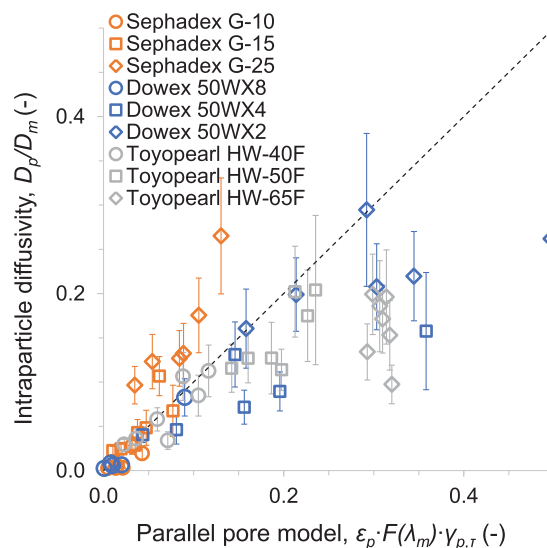

Fig. 6. Correlation of measured intraparticle diffusivity to the parallel pore model: product of particle porosity ε_p, hindrance diffusion factor $F(\lambda_m)$, and internal obstruction factor $\gamma_{p,\tau}$.

ties of *Sephadex* and *Toyopearl* stationary phases are very similar. The *Dowex* stationary phase series shows the largest $\gamma_{p,\tau}$, which may be due to the fact that the ionic surface charge on the ion-exchange stationary phase reduces impedance. Measured obstruction factors can be found in Table 18, Table 19, and Table 20 in the supplementary material.

4.7. The parallel pore model

Correlating intraparticle diffusion to individual stationary phase properties, as defined in the parallel pore model, in combination with properties of the diffusing molecules did not lead to a conclusive correlation. In Fig. 6 we show the correlation of measured intraparticle diffusivities to the product of particle porosity, hindrance to diffusion, and internal obstruction factor, the parallel pore model.
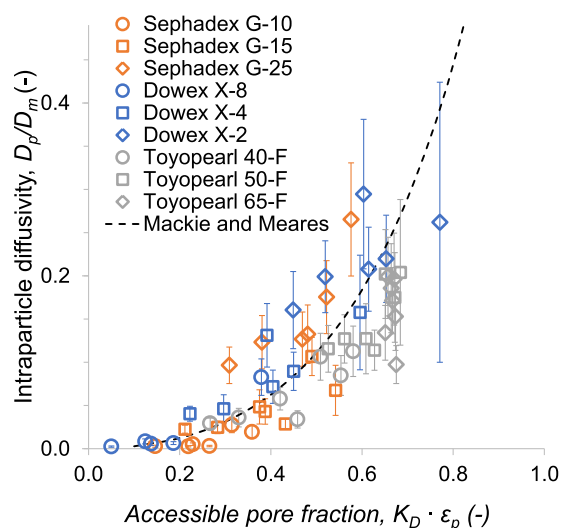
Fig. 7. Accessible fraction of pore volume, calculated from the product of K_D and particle porosity.

Bringing together all three parameters of the parallel pore model in the relation to measured intraparticle diffusivity lead to reasonably accurate predictions for small intraparticle diffusivities ($D_p/D_m < 0.2$), with the exception of *Sephadex* G-25. The data appeared to "level off" for larger intraparticle diffusivities. Generally, intraparticle diffusion in the *Sephadex* series appeared to be underestimated, while the *Dowex* and *Toyopearl* data appeared to be overestimated.

In comparison to the simple correlation of Mackie and Meares (Fig. 3a), the parallel pore model is an improvement. It provides more insight into the interplay of geometric properties between stationary phase and diffusing molecule and the predictability of the intraparticle diffusivity increases. However, based on Fig. 6 it is not possible to predict the intraparticle diffusivity over the whole measurement range, even though the parallel pore model considers more data. We have attempted to find an explicit correlation between intraparticle diffusivity and pore characteristics, but not all model input parameters were experimentally measurable. As with all models that serve to simplify reality, the projection deviates from physical reality. Within the parallel pore model reality is simplified by the use of lumped parameters, to describe mass transfer within the porous networks. The pore structures shown in Fig. 2 are interpreted as parallel pores, with interconnections between the pores. The calculation of molecular radii, to determine molecule sizes, may not capture the true effect molecular shape has on diffusivity in constricted spaces. Furthermore the hindrance diffusion factor $F(\lambda_m)$, based on a mean pore radius and relying on the molecular radius, could be inaccurate for different shapes of pores and molecules. And the tortuosity, which is measured via electric conductivity, may vary from the tortuosity a given molecule encounters inside the porous structures. It is possible that pore structure is a topic more complex than captured in the three parameters of the parallel pore model.

4.8. Accessible fraction of pore volume and its influence on intraparticle diffusivity

In an attempt to relate measured intraparticle diffusivities more accurately to pore characteristics, the accessible fraction of pore volume for each molecule was calculated from the product of K_D and particle porosity ε_p. Here, K_D was calculated with Eq. (14) for each molecule and stationary phase. Plotted against measured intraparticle diffusivity the accessible fraction of pore volume yields an exponential trend that follows the trend predicted by Mackie

and Meares (Fig. 7), which in this case should be interpreted according to Eq. (19).

$$D_P = \left[\frac{K_D \varepsilon_P}{2 - K_D \varepsilon_P}\right]^2 D_m \tag{19}$$

This method yields a clear correlation between measured intraparticle diffusivities and pore characteristics and provides a predictive model. The main advantage of this predictive model is that it relies only on ISEC measurements that can be collected from a packed column, in which the stationary phase is in the same conditions as during the anticipated separation process. Furthermore, the use of the accessible fraction of pore volume does not rely on absolute pore dimensions, as it relies on data recorded with the same or similar molecules. The proposed equation should be further challenged, specifically widening the applicability to higher accessible pore fractions (> 0.7) with corresponding higher intraparticle diffusivities ($D_p/D_m > 0.2$).

5. Conclusions

Measured intraparticle diffusivity (D_p/D_m) in this work ranged from 0.02 to 0.2, with a few exceptions. If a first estimate is required, it seems reasonable to assume diffusion inside a porous chromatographic particle to be around 10% of the bulk diffusion, as suggested by Nicoud [16] and Ruthven [21]. When the particle porosity is known, a better estimate is obtained with the Mackie and Meares correlation. Although, on average, it overestimates intraparticle diffusivity by a factor of three. Including further characterization of the resin by measuring the mean pore size, the internal obstruction factor and the hindrance diffusion factor, the parallel pore model can provide a better insight and prediction of the intraparticle diffusivity. However, the best prediction of the intraparticle diffusivity to stationary phase characteristics was obtained by using the Mackie and Meares correlation in combination with the apparent fraction of accessible pore volume. This approach should be further challenged, specifically widening the applicability to higher accessible pore fractions (>0.7) with corresponding higher intraparticle diffusivities ($D_p/D_m > 0.2$).

Declaration of Competing Interest

The authors declare that they have no known competing financial interests or personal relationships that could have appeared to influence the work reported in this paper.

CRediT authorship contribution statement

A. Schultze-Jena: Conceptualization, Methodology, Investigation, Formal analysis, Writing - original draft, Data curation. **M.A. Boon:** Conceptualization, Supervision, Writing - review & editing. **D.A.M. de Winter:** Investigation, Writing - review & editing. **P.J.Th. Bussmann:** Supervision, Writing - review & editing. **A.E.M. Janssen:** Supervision, Writing - review & editing. **A. van der Padt:** Supervision, Writing - review & editing.

Acknowledgments

Supplementary materials

Supplementary material associated with this article can be found, in the online version, at doi:10.1016/j.chroma.2019.460688.

References

[1] V.E. Barsky, A.M. Kolchinsky, Y.P. Lysov, A.D. Mirzabekov, Biological microchips with hydrogel-immobilized nucleic acids, proteins, and other compounds: properties and applications in genomics, Mol. Biol. 36 (2002) 437–455.

[2] T.-O. Peulen, K.J. Wilkinson, Diffusion of nanoparticles in a biofilm, Environ. Sci. Technol. 45 (2011) 3367–3373.

[3] N. Murthy, Y.X. Thng, S. Schuck, M.C. Xu, J.M.J. Fréchet, A novel strategy for encapsulation and release of proteins: hydrogels and microgels with acid-labile acetal cross-linkers, J. Am. Chem. Soc. 124 (2002) 12398–12399.

[4] S. Sershen, J. West, Implantable, polymeric systems for modulated drug delivery, Adv. Drug Deliv. Rev. 54 (2002) 1225–1235.

[5] O. Wichterle, D. LÍM, Hydrophilic gels for biological use, Nature 185 (1960) 117–118.

[6] H.-W. Kang, Y. Tabata, Y. Ikada, Fabrication of porous gelatin scaffolds for tissue engineering, Biomaterials 20 (1999) 1339–1344.

[7] A.S. Hoffman, Hydrogels for biomedical applications, Adv. Drug Deliv. Rev. 54 (2002) 3–12.

[8] A.Z. Abidin, T. Puspasari, W.A. Nugroho, Polymers for enhanced oil recovery technology, Procedia Chem. 4 (2012) 11–16.

[9] R. Zolfaghari, A.A. Katbab, J. Nabavizadeh, R.Y. Tabasi, M.H. Nejad, Preparation and characterization of nanocomposite hydrogels based on polyacrylamide for enhanced oil recovery applications, J. Appl. Polym. Sci. 100 (2006) 2096–2103.

[10] D.A.M. de Winter, F. Meirer, B.M. Weckhuysen, FIB-SEM tomography probes the mesoscale pore space of an individual catalytic cracking particle, ACS Catal. 6 (2016) 3158–3167.

[11] P. Dechadilok, W.M. Deen, Hindrance factors for diffusion and convection in pores, Ind. Eng. Chem. Res. 45 (2006) 6953–6959.

[12] S.T. Balke, A.E. Hamielec, B.P. LeClair, S.L. Pearce, Gel permeation chromatography, Ind. Eng. Chem. Prod. Res. Dev. 8 (1969) 54–57.

[13] Y. Yao, A.M. Lenhoff, Determination of pore size distributions of porous chromatographic adsorbents by inverse size-exclusion chromatography, J. Chromatogr. A 1037 (2004) 273–282.

[14] L. Shen, Z. Chen, Critical review of the impact of tortuosity on diffusion, Chem. Eng. Sci. 62 (2007) 3748–3755.

[15] B. Ghanbarian, A.G. Hunt, R.P. Ewing, M. Sahimi, Tortuosity in porous media: a critical review, Soil Sci. Soc. Am. J. 77 (2013) 1461.

[16] R.M. Nicoud, Chromatographic Processes, Cambridge University Press, 2015.

[17] M. Schröder, E. von Lieres, J. Hubbuch, Direct quantification of intraparticle protein diffusion in chromatographic media, J. Phys. Chem. B 110 (2006) 1429–1436.

[18] G. Guiochon, D.G. Shirazi, A. Felinger, A.M. Katti, Fundamentals of Preparative and Nonlinear Chromatography, Academic Press, 2006.

[19] D. Sandrin, D. Wagner, C.E. Sitta, R. Thoma, S. Felekyan, H.E. Hermes, C. Janiak, S.A. de R. Kuhnemuth, H. Lowen, S.U. Egelhaaf, C.A.M. Seidel, Diffusion of macromolecules in a polymer hydrogel: from microscopic to macroscopic scales, Phys. Chem. Chem. Phys. 18 (2016) 12860–12876.

[20] P. Dechadilok, W.M. Deen, Hindrance factors for diffusion and convection in pores, Ind. Eng. Chem. Res. 45 (2006) 6953–6959.

[21] J. Kärger, D.M. 4390, D.N. Theodorou, Diffusion in Nanoporous Materials, 2, Wiley, 2012 Volume Set.

[22] A.G. Ogston, B.N. Preston, J.D. 5541, On the transport of compact particles through solutions of chain-polymers, Proc. R. Soc. Lond. A 333 (1973) 297–316.

[23] R. Taylor, R. Krishna, Multicomponent Mass Transfer, Wiley, New York, 1993.

[24] C.N. Satterfield, C.K. Colton, W.H. Pitcher, Restricted diffusion in liquids within fine pores, AIChE J. 19 (1973) 628–635.

[25] H. Brenner, L.J. Gaydos, The constrained Brownian movement of spherical particles in cylindrical pores of comparable radius. Models of the diffusive and convective transport of solute molecules in membranes and porous media, J. Colloid Interface Sci. 58 (1977) 312–356.

[26] F. Gritti, G. Guiochon, Mass transfer kinetics, band broadening and column efficiency, J. Chromatogr. A 1221 (2012) 2–40.

[27] B. Coquebert de Neuville, A. Tarafder, M. Morbidelli, Distributed pore model for bio-molecule chromatography, J. Chromatogr. A 1298 (2013) 26–34.

[28] J. van Brakel, P.M. Heertjes, Analysis of diffusion in macroporous media in terms of a porosity, a tortuosity and a constrictivity factor, Int. J. Heat Mass Transf. 17 (1974) 1093–1103.

[29] C.N. Satterfield, Mass Transfer in Heterogeneous Catalysis, M.I.T. Press, 1970.

[30] M. Suzuki, Adsorption Engineering, Kodansha, 1990.

[31] K. Miyabe, G. Guiochon, Measurement of the parameters of the mass transfer kinetics in high performance liquid chromatography, J. Sep. Sci. 26 (2003) 155–173.

[32] B. Coquebert de Neuville, H. Thomas, M. Morbidelli, Simulation of porosity decrease with protein adsorption using the distributed pore model, J. Chromatogr. A 1314 (2013) 77–85.

[33] Y. Yao, K.J. Czymmek, R. Pazhianur, A.M. Lenhoff, Three-dimensional pore structure of chromatographic adsorbents from electron tomography, Langmuir 22 (2006) 11148–11157.

[34] G. Carta, A. Jungbauer, in: Adsorption Kinetics, Protein Chromatography, Wiley-VCH Verlag GmbH & Co. KGaA, 2010, pp. 161–199.

[35] F. Gritti, G. Guiochon, General HETP equation for the study of mass-transfer mechanisms in RPLC, Anal. Chem 78 (2006) 5329–5347.

[36] E.M. Renkin, Filtration, diffusion, and molecular sieving through porous cellulose membranes, J. Gen. Physiol. 38 (1954) 225–243.

[37] F. Gritti, G. Guiochon, Effect of the surface coverage of C18-bonded silica particles on the obstructive factor and intraparticle diffusion mechanism, Chem. Eng. Sci. 61 (2006) 7636.

[38] S. Khirevich, A. Höltzel, A. Daneyko, A. Seidel-Morgenstern, U. Tallarek, Structure–transport correlation for the diffusive tortuosity of bulk, monodisperse, random sphere packings, J. Chromatogr. A 1218 (2011) 6489–6497.

[39] N. Epstein, On tortuosity and the tortuosity factor in flow and diffusion through porous media, in: Chemical Engineering Science, 1989, pp. 777–779.

[40] J.C. Giddings, Dynamics of Chromatography: Principles and Theory, CRC Press, 2017.

[41] S. Chalk, L. McEwen, in: The IUPAC Gold Book, Chemistry International, 2017, p. 39.

[42] F. Gritti, G. Guiochon, Application of the general height equivalent to a theoretical plate equation to size exclusion chromatography. Study of the mass transfer of high-molecular-mass compounds in liquid chromatography, Anal. Chem. 79 (2007) 3188–3198.

[43] J.J. Meyers, A.I. Liapis, Network modeling of the intraparticle convection and diffusion of molecules in porous particles packed in a chromatographic column, J. Chromatogr. A 827 (1998) 197–213.

[44] J.C. Giddings, Dynamics of Chromatography. Part. I: Principles and Theory, Marcel Dekker, New York, 1965.

[45] D. Wiedenmann, L. Keller, L. Holzer, J. Stojadinović, B. Münch, L. Suarez, B. Fumey, H. Hagendorfer, R. Brönnimann, P. Modregger, M. Gorbar, U.F. Vogt, A. Züttel, F.L. Mantia, R. Wepf, B. Grobéty, Three-dimensional pore structure and ion conductivity of porous ceramic diaphragms, AIChE J. 59 (2013) 1446–1457.

[46] M. Barrande, R. Bouchet, R. Denoyel, Tortuosity of porous particles, Anal. Chem 79 (2007) 9115–9121.

[47] P. Aggarwal, V. Asthana, J.S. Lawson, H.D. Tolley, D.R. Wheeler, B.A. Mazzeo, M.L. Lee, Correlation of chromatographic performance with morphological features of organic polymer monoliths, J. Chromatogr. A 1334 (2014) 20–29.

[48] K. Diao, L. Zhang, Y. Zhao, Measurement of tortuosity of porous Cu using a diffusion diaphragm cell, Measurement 110 (2017) 335–338.

[49] J. Landesfeind, J. Hattendorff, A. Ehrl, W.A. Wall, H.A. Gasteiger, Tortuosity determination of battery electrodes and separators by impedance spectroscopy, J. Electrochem. Soc 163 (2016) A1373–A1387.

[50] M. Matyka, Z. Khalili, Z. Koza, Tortuosity-porosity relation in porous media flow, Phys. Rev. E 78 (2008) 1–8.

[51] I.V. Thorat, D.E. Stephenson, N.A. Zacharias, K. Zaghib, J.N. Harb, D.R. Wheeler, Quantifying tortuosity in porous Li-ion battery materials, J. Power Sour. 188 (2009) 592–600.

[52] L. Chen, L. Chen, X. Yan, Q.-H. Wan, Measurement of packing tortuosity and porosity in capillary electrochromatography, Anal. Chem. 74 (2002) 5157–5159.

[53] G.M. Laudone, C.M. Gribble, K.L. Jones, H.J. Collier, G.P. Matthews, Validated a priori calculation of tortuosity in porous materials including sandstone and limestone, Chem. Eng. Sci. 131 (2015) 109–117.

[54] N.O. Shanti, V.W.L. Chan, S.R. Stock, F. De Carlo, K. 3647, K.T. Faber, X-ray micro-computed tomography and tortuosity calculations of percolating pore networks, Acta Mater. 71 (2014) 126–135.

[55] I.V. Thorat, D.E. Stephenson, N.A. Zacharias, K. Zaghib, J.N. Harb, D.R. Wheeler, Quantifying tortuosity in porous Li-ion battery materials, J. Power Sources (2009) 592–600.

[56] B. Tjaden, D.P. Finegan, J. Lane, D.J.L. Brett, P.R. Shearing, Contradictory concepts in tortuosity determination in porous media in electrochemical devices, Chem. Eng. Sci. (2017) 235–245.

[57] Y. Yao, K.J. Czymmek, R. Pazhianur, A.M. Lenhoff, Three-dimensional pore structure of chromatographic adsorbents from electron tomography, Langmuir 22 (2006) 11148–11157.

[58] J.J. Meyers, S. Nahar, D.K. 5214, A.I. Liapis, Determination of the pore connectivity and pore size distribution and pore spatial distribution of porous chromatographic particles from nitrogen sorption measurements and pore network modelling theory, J. Chromatogr. A 907 (2001) 57–71.

[59] J.F. Langford, M.R. Schure, Y. Yao, S.F. Maloney, A.M. Lenhoff, Effects of pore structure and molecular size on diffusion in chromatographic adsorbents, J. Chromatogr. A 1126 (2006) 95–106.

[60] L. Hagel, Chapter 5 Pore size distributions, in: P.L. Dubin (Ed.), Journal of Chromatography Library, Elsevier, 1988, pp. 119–155.

[61] S. Ergun, Fluid Flow Through Packed Columns, 48, Chemical Engineering Progress, 1952.

[62] A. Schultze-Jena, M.A. Boon, P.J.T. Bussmann, A.E.M. Janssen, A. van der Padt, The counterintuitive role of extra-column volume in the determination of column efficiency and scaling of chromatographic processes, J. Chromatogr. A 1493 (2017) 49–56.

[63] J.J. Baeza-Baeza, S. Pous-Torres, J.R. Torres-Lapasió, M.C. García-Álvarez-Coque, Approaches to characterise chromatographic column performance based on global parameters accounting for peak broadening and skewness, J. Chromatogr. A 1217 (2010) 2147–2157.

[64] A.J. 3568, T.J. Waeghe, K.W. Himes, F.P. Tomasella, T.F. Hooker, Modifying conventional high-performance liquid chromatography systems to achieve fast separations with Fused-Core columns: a case study, J. Chromatogr. A 1218 (2011) 5456–5469.

[65] F. Gritti, A. Felinger, G. Guiochon, Influence of the errors made in the measurement of the extra-column volume on the accuracies of estimates of the column efficiency and the mass transfer kinetics parameters, J. Chromatogr. A 1136 (2006) 57–72.

[66] D.S. Eisenberg, W. Kauzmann, The Structure and Properties of Water, Clarendon Press; Oxford University Press, Oxford, New York, 2005.

[67] R.C. Reid, J.M. Prausnitz, B.E. Poling, The Properties of Gases and Liquids, 1987.

[68] E.J. Wilson, C.J. Geankoplis, Liquid mass transfer at very low reynolds numbers in packed beds, Ind. Eng. Chem. Fund. 5 (1966) 9–14.

[69] P. DePhillips, A.M. Lenhoff, Pore size distributions of cation-exchange adsorbents determined by inverse size-exclusion chromatography, J. Chromatogr. A 883 (2000) 39–54.

[70] L. Hagel, M. Östberg, T. Andersson, Apparent pore size distributions of chromatography media, J. Chromatogr. A 743 (1996) 33–42.

[71] A.L. Zydney, P. Aimar, M. Meireles, J.M. Pimbley, G. Belfort, Use of the log-normal probability density function to analyze membrane pore size distributions: functional forms and discrepancies, J. Membr. Sci 91 (1994) 293–298.

[72] K. Horváth, D. Lukács, A. Sepsey, A. Felinger, Effect of particle size distribution on the separation efficiency in liquid chromatography, J. Chromatogr. A 1361 (2014) 203–208.

[73] G.E. Healthcare, Column Efficiency Testing, 2010 https://www.gelifesciences.com.

[74] J.C. Williams, L.A. Mark, S. Eichholtz, Partition and permeation of dextran in polyacrylamide gel, Biophys. J. (1998) 493–502.

[75] J. Gutenwik, B. Nilsson, A. Axelsson, Effect of hindered diffusion on the adsorption of proteins in agarose gel using a pore model, J. Chromatogr. A 1048 (2004) 161–172.

[76] T. Bioscience, TOYOPEARL® Instruction Manual, 2015 https://www.separations.eu.tosohbioscience.com.